SCIENTIFIC REPORTS

OPEN

SUBJECT AREAS:
SYNTHESIS AND PROCESSING
PHOTOCATALYSIS
CHEMICAL ENGINEERING
POROUS MATERIALS

Received
29 April 2013

Accepted
4 October 2013

Published
22 October 2013

Correspondence and requests for materials should be addressed to R.Z. (zhangruidavid1@gmail.com) or X.S. (shaoxia@sit.edu.cn)

Enhanced photocatalytic activity of TiO_2-C hybrid aerogels for methylene blue degradation

Xia Shao[1,2], Wencong Lu[2], Rui Zhang[1] & Feng Pan[1]

[1]School of Materials Science and Engineering, Shanghai Institute of Technology, Shanghai 201418, China, [2]School of Materials Science and Engineering, Shanghai University, Shanghai 200444, China.

Carbon-based TiO_2 composites have many advantages as photocatalysts. However, they suffer from low light efficiency due to the low contrast of TiO_2 with carbon. We synthesized a novel type of anatase-type TiO_2-C hybrid aerogel by a one-pot sol-gel method, which shows a photocatalytic activity for methylene degradation up to 4.23 times that of P25, a commercial photocatalyst from Degussa Inc. The hybrid aerogels are prepared from $TiCl_4$ and resorcinol–furfural, and have a tunable macropore size from 167 to 996 nm. They are formed of submicrometer particles that consist of interwoven anatase and carbon nanoparticles. The anatase nanoparticles have a size of 8–9 nm and a tunable oxygen vacancy from 7.2 to 18.0%. The extremely high activity is ascribed to the large light absorption caused by macropore scattering and oxygen vacancies in the anatase. These findings may open up a new avenue and stimulate further research to improve photocatalytic performance.

Titanium dioxide (TiO_2) has attracted much attention as a semiconducting photocatalyst for pollution abatement in water or air, owing to its strong oxidizing power, abundance, low cost, high chemical inertness and photostability. Its structure-property relationships have been extensively investigated, and these reveal that phase type[1], particle size[2], surface hydrophilicity[3], crystallinity[4], morphology[5] and oxygen vacancy concentration[6,7] have a great influence in its photocatalytic activity. But it still suffers from low efficiency and a narrow light response range if it is used alone. Many efforts have been made by forming composites or hybridizing TiO_2 with other materials to overcome these drawbacks, such as combining the photocatalytic activity of TiO_2 with the adsorptivity of porous carbons[8–10], reducing electron–hole recombination rate[11] and doping to achieve a narrow band gap[12–16]. TiO_2-carbon (TiO_2-C) hybrids are some of the most extensively investigated and most promising materials to improve the photocatalytic performance of TiO_2 because a variety of carbon materials can be tailor-made to meet the demands of TiO_2 as a photocatalyst. In addition, the lightweight, nonpolar, nonreactive and nontoxic nature of carbon materials and the easy separation of the materials from water are attractive in waste water treatment. There are three types of TiO_2-C hybrids, carbon-supported, carbon doped and carbon coated TiO_2[17], from which many beneficial features have been obtained.

The detailed mechanism of the photocatalytic process on the TiO_2 surface is still not completely clear, particularly that concerning the initial steps involved in the reaction of reactive oxygen species and organic molecules[18]. A reasonable assumption is that both photocatalytic oxidative and reductive reactions occur simultaneously on the TiO_2 particle. When the electrons in TiO_2 (anatase phase) are irradiated by UV rays they can be excited from the valence band to the conduction band to generate electron–hole pairs. The holes created in the valence band can react with water molecules to give hydroxide radicals $^{\cdot}OH$ and the photogenerated electrons are sufficiently reduced to produce superoxide (O_2^{-}). The redox potential of the electron–hole pair permits H_2O_2 formation. Depending on the reaction conditions, the holes, $^{\cdot}OH$ radicals, O_2^{-}, H_2O_2, and O_2 can play important roles in the photocatalytic reaction mechanism. There are several issues that are important in this process. First, exposing the external surface of TiO_2 particles to light is a prerequisite to make such an excitement happen. Second, the light energy ($E = h\nu$) must exceed the band gap (3.20 eV) of the anatase-type TiO_2, therefore lowering the band gap of TiO_2 or using low wave length light is needed to increase the light utilization efficiency. Third, the oxidizing species cannot migrate for a long distance and stay near the active centers in the TiO_2 particles. Therefore, polluting molecules have to diffuse to the photo-excited active centers. Fourth, the recombination of positive holes with excited electrons before they react to create active species and centers has to be avoided. Moreover, the TiO_2 loaded in the composites should not decrease under repeated cycles and must be easy to separate from water from a commercial application point of view.

Most of these issues can be circumvented by hybridizing TiO_2 with carbon materials. Loading TiO_2 nanoparticles on the surface of activated carbons/activated carbon fibers or mixing the two can significantly increase the photocatalytic activity for methylene blue (MB) degradation in aqueous solutions[19–21], which can be ascribed to a decreased diffusion path of MB to the active centers by adsorption of MB from the bulk solution by the activated carbon. The interaction of carbon with TiO_2 can effectively inhibit TiO_2 particle growth and simultaneously increase crystallinity during heat treatment by suppressing the phase transformation from photoactive anatase to less active rutile[22]. Cationic[23] and anionic[16,24,25] doping of TiO_2 by carbon have been reported to narrow its band gap and significantly enhance catalytic activity in the visible light region. The presence of graphene[13] or carbon nanotubes[26] in TiO_2-based nanocomposites can effectively inhibit the electron-hole pair recombination, lower the band gap of TiO_2, increase the adsorptivity of pollutants, and decrease light weakening due to a small number of graphene layers and therefore a decreased light absorption by carbon as compared with other forms of carbons.

However, in most cases, not all of these issues can be resolved simultaneously, and a compromise must be made because solving some of the problems could make others worse. For example, the coating layer in carbon-coated TiO_2[27] increases adsorptivity, but decreases the light intensity irradiated on TiO_2. The former favors catalytic activity while the latter is detrimental. As a compromise, maximum photocatalytic activity is obtained by increasing the thickness of the coating-layer. The carbon layer has a high light absorption that weakens the light intensity arriving at catalyst surface, and this limits the increase in the efficiency of the present TiO_2-C hybrids. Therefore, a state-of-the-art design of TiO_2-based hybrids is important for their further improvement.

There are several methods to prepare carbon-based TiO_2 hybrids, including chemical vapor deposition of alkoxide precursors[28], impregnation of a sol prepared by alkoxide hydrolysis into activated carbon[29,30], loading of a powder prepared in advance directly onto activated carbon[31], a sol-gel approach[32,33], hybridizing with nanocarbons such as carbon nanotubes[34] or graphene[13], etc. The first three methods normally produce TiO_2 particles coated on the external surface or at pore entrances of the activated carbon particles. Adsorbed molecules have to diffuse to the external surface of the composite particles in order to achieve contact with the active sites on the TiO_2 particles. Therefore, for these hybrid materials the diffusion paths for the targeted molecules are longer than for carbon nanotube or graphene-based composite materials that are homogeneous at the nanometer scale. The sol-gel approach allows for a nanometer scale mixing of TiO_2 nanoparticles with carbon nanoparticles, which is advantageous in this regard. In addition, the microstructure of the sol-gel derived composite materials can be tailored with a wide range of length scale from nanometer to micrometer, which makes it possible for a targeted textural control. Moreover, the nanometer scale mixing of TiO_2 with carbon can prevent TiO_2 particles from falling off the carbon, which is advantageous in industrial applications.

In this paper, a novel type of TiO_2-C hybrid aerogels was synthesized by one-pot sol-gel approach. The hybrid aerogels have dominant macropores and a small fraction of micro and mesopores, but show much higher photocatalytic activities for MB degradation under UV irradiation than P25, a commercial TiO_2 (Degussa Co., Ltd., Germany). The reasons for the enhanced performance and the factors affecting the photocatalytic activity of this kind of hybrid material are analyzed.

Results

Crystalline structure. Fig. 1a shows powder X-ray diffraction (XRD) patterns of the TiO_2-C hybrid aerogels. The peaks at 25.5°, 37.8°, 48.3°, 54.1° and 62.8° can be ascribed to the (101), (004), (200), (105) and (204) plane of anatase, respectively. There are no peaks found

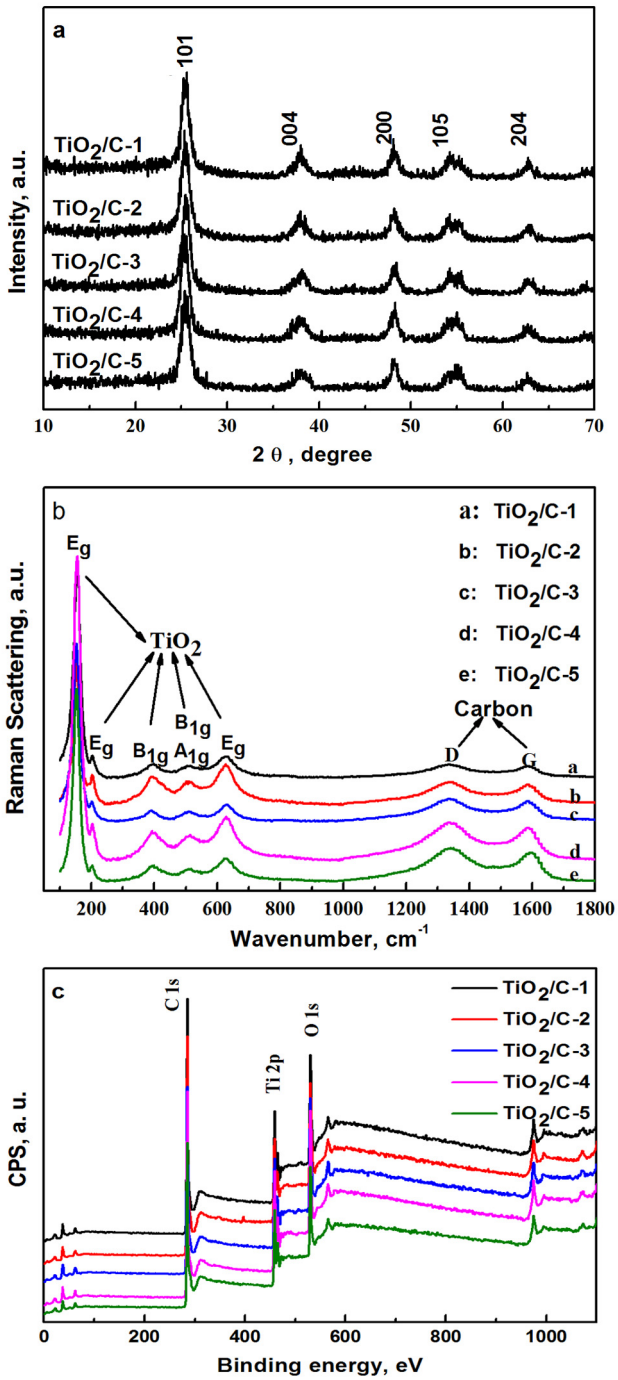

Figure 1 | a) XRD patterns, b) Raman spectra and c) XPS spectra of the TiO_2-C hybrid aerogels.

that belong to the rutile phase or graphite. The absence of graphite peaks indicates that the carbon is in an amorphous state. The absence of rutile is reasonable because carbon suppresses the phase transition from anatase to rutile as revealed in carbon-supported[29] and carbon-coated TiO_2[22] even if the samples are carbonized at 800°C. It should be noted that the half-width at half maximum (FWHM) of (101) peaks and the crystallite size of anatase obtained from the peaks by the Scherrer equation are the same within experimental error (8.0–8.6 nm) for all samples investigated (Table 1). This may be due to the same procedure and processing conditions being used for all these samples. The TiO_2 contents in the TiO_2-C hybrid aerogels increase with the mass ratio of $TiCl_4$ to resorcinol (R) and furfural (F), $TiCl_4$/(R + F) as expected. The FWHMs of the (101) peaks are around

Table 1 | Microstructure parameters of the TiO_2-C hybrid aerogels

	TiO_2-C-1	TiO_2-C-2	TiO_2-C-3	TiO_2-C-4	TiO_2-C-5
$TiCl_4$/(R + F), wt/wt	0.629	0.720	0.902	1.171	1.261
TiO_2 content, wt%	25.3	31.2	40.1	48.1	50.2
FWHM,°(101 peak)	0.96 ± 0.05	0.94 ± 0.05	1.00 ± 0.05	1.01 ± 0.05	0.97 ± 0.05
Crystalline size, nm	8.4 ± 0.6	8.6 ± 0.6	8.1 ± 0.6	8 ± 0.6	8.3 ± 0.6
Micropore volume, cm^3/g	0.017	0.043	0.026	0.023	0.014
S_{BET}, m^2/g	237	160	204	180	192
Mesopore volume, cm^3/g	0.058	0.054	0.085	0.073	0.080
External surface area, m^2/g	188.3	88.5	91.8	91.5	116.7
V_{Hg}, cm^3/g	2.04	2.04	1.62	1.70	1.85

0.97°, indicating that the peaks are very broad, which is attributed to the very small particle sizes of anatase.

Fig. 1b shows the Raman spectra of the TiO_2-C hybrid aerogels. The peaks at 1338 and 1587 cm^{-1} can be ascribed to D and G bands of carbon respectively. Sharp Raman peaks are seen at around 153 cm^{-1}, shoulder peaks at 202 cm^{-1} and three broader peaks in the high frequency region located at around 398, 514 and 626 cm^{-1}. Anatase has a space group D_{4h} ($I4_1/amd$) with six Raman active vibrational modes, $A_{1g} + 2B_{1g} + 3E_g$. The six allowed bands in the first-order Raman spectrum are located at 144 (E_g), 197 (E_g), 399 (B_{1g}), 513 (A_{1g}), 519 (B_{1g}) and 639 (E_g) cm^{-1}. All the Raman features observed in the spectra are close to those of the single crystal anatase phase as shown in Table 2. It is evident that the TiO_2-C hybrid aerogels possess a certain degree of long-range order of the anatase phase and that no observable rutile features are found. It is found that the E_g peaks at 144 and 639 cm^{-1} are blue-shifted and red-shifted to around 153 and 626 cm^{-1}, respectively as compared with single crystal anatase. The E_g peak at 197 cm^{-1} is blue shifted to around 203 cm^{-1}. The red shifts of the B_{1g} and A_{1g} peaks at 399 and 519 cm^{-1} all exhibit a maximum at $TiCl_4$/(R + F) of 0.902, i.e. sample TiO_2-C-3. The apparent blue and red shifts are related to the lower crystal size[35], number of oxygen vacancies[36] and pressure[37] in the anatase phase.

Fig. 1c contains the XPS spectra of the TiO_2-C hybrid aerogels, showing the presence of elemental C, O, Ti for all samples and of N in TiO_2-C-2. The deconvolutions and assignments of the peaks in the Ti 2p, O 1s, C 1s and N 1s spectra are shown in Fig. S1 and Tables S1, S2 and S3. The spin-orbit splitting of the Ti 2p leads to two 2p peaks located at 459.0 and 464.7 eV, which can be ascribed to Ti $2p_{3/2}$ and Ti $2p_{1/2}$, respectively. From the peak positions[38], it can be concluded that the Ti in the hybrid aerogels is predominantly Ti^{4+}. For the TiO_2-C-2 sample, a shoulder is found near Ti $2p_{3/2}$, which can be attributed to the TiN(oxide)[39] with its Ti $2p_{3/2}$ and Ti $2p_{1/2}$ peaks located at 457.3 and 463.0 eV respectively. It is not clear why TiO_2-C-2 has small amount of nitrogen while other samples do not. The O 1s spectra can be fitted by three chemical states at 530.2–530.4, 531.3 and 533.2 eV, which can be ascribed to O in the form of O-Ti, C-O-C and O=C, respectively. From the O-Ti percentages from the O 1s spectra and the O and Ti atom ratios from the XPS overview spectra, we can estimate the number of O atoms bonded with Ti^{4+}, e.g x in TiOx (Table 3). It is found that x values of the anatase phase in all samples varies from 1.64 to 1.86, all of which are non-stoichiometric (less than 2), which corresponds to oxygen vacancy concentrations from 18.0 to 7.2%. The C 1s spectra can be deconvoluted into the following bands based on the literature[40]. The main peak at 284.5 eV can be assigned to sp^2 hybridized C atoms, while the higher energy peaks arise from sp^3 hybridized C at 285.7 eV, C-O-C at 287.1 eV, C=O at 288.7 eV, and the shakeup line of carbon in aromatic compounds at 290.5 eV (π-π*). The oxygen functional groups from C 1s spectra agree with those from O 1s spectra. It should be mentioned that the phenol group in resorcinol is not retained in carbon and converted to C=O group, which might be caused by oxidation of phenol group by TiO_2 at high temperature.

There are rough agreements between XPS and Raman results. The sample TiO_2-C-3 has the lowest oxygen vacancy concentration. The Raman blue shift of TiO_2-C-3 at 144 cm^{-1} exhibit a minimum and its red shifts of the B_{1g} and A_{1g} peaks at 399 and 519 cm^{-1} all exhibit a maximum. It was reported that the Raman blue shift of E_g at 144 cm^{-1} increases with oxygen vacancy concentration and levels off above 5% for nanophase anatase[36]. This can explain why there is no noticeable difference between shifts of the E_g peak at 144 cm^{-1} although our samples have a wide range of oxygen vacancy concentration (7.2–18.0%). The incomplete agreement between the XPS and Raman results for all samples might be caused by the pressure[37] that the carbon structure exerts on anatase, resulting from volume shrinkage of the carbon precursors during carbonization, which is impossible to control.

Structure and porosity. Fig. 2 shows SEM, TEM and HRTEM images of the TiO_2-C hybrid aerogels. SEM and TEM show that they are formed by large aggregates that form macropores. The average size of the aggregates decreases from 268 to 216 nm with increasing $TiCl_4$/(R + F) ratio. The aggregates in SEM images can be seen in more detail by TEM that they are formed of TiO_2 and carbon nanoparticles. The black regions in the TEM images are TiO_2 particles because TiO_2 has a higher electron density and therefore a higher contrast than carbon. It is clear that TiO_2 particles of 8–9 nm are distributed discretely within the carbon, which is in agreement with the particle sizes calculated from XRD. However, we have found that the carbon and anatase are bicontinuous and interwoven, each not coated by the other in the hybrid aerogels from the fact that the TiO_2-C hybrid aerogels retain their monolithic shape after burning in air at 600°C to remove the carbon or leaching in HF

Table 2 | Raman vibrational modes, their shifts and linewidths

Samples	E_g, cm^{-1}	FWHM, cm^{-1}	E_g, cm^{-1}	B_{1g}, cm^{-1}	$A_{1g}+B_{1g}$, cm^{-1}	E_g, cm^{-1}
Single crystal anatase	144	---	197	399	513 + 519	639
Single crystal rutile	447	---	612	143	826(B_{2g})	---
TiO_2-C-1	155 ± 1	27 ± 1	203 ± 4	398 ± 4	518 ± 4	625 ± 4
TiO_2-C-2	154 ± 1	25 ± 1	202 ± 4	396 ± 4	509 ± 4	626 ± 4
TiO_2-C-3	153 ± 1	25 ± 1	202 ± 4	392 ± 4	508 ± 4	626 ± 4
TiO_2-C-4	155 ± 1	29 ± 1	203 ± 4	400 ± 4	514 ± 4	627 ± 4
TiO_2-C-5	153 ± 1	25 ± 1	203 ± 4	398 ± 4	514 ± 4	625 ± 4

Table 3 | Atom ratios, contents of oxygen bonded with Ti and carbon, and oxygen vacancy from X-ray photoelectron spectroscopy

Samples	C	Ti	O	N	Ti(N)	Ti(O)	O(Ti)	x in	Oxygen	O(C)/C
		at%			at%	at%	at%	TiOx	vacancy,%	at/at
TiO_2-C-1	74.83	6.90	18.27	0	0	6.90	11.89	1.72	13.8	0.085
TiO_2-C-2	74.60	7.40	16.90	1.10	1.10	6.40	10.73	1.68	16.2	0.083
TiO_2-C-3	72.87	7.75	19.37	0	0	7.75	14.39	1.86	7.2	0.068
TiO_2-C-4	72.70	8.10	19.20	0	0	8.10	14.19	1.75	12.4	0.069
TiO_2-C-5	72.61	8.30	19.08	0	0	8.30	13.61	1.64	18.0	0.075

to remove TiO_2 as shown in Fig. S2. The size of TiO_2 particles increases significantly after the hybrid aerogels are burned in air, which is caused by crystal growth and sintering at high temperature. The carbon structure remains unchanged after the leaching with HF. This disagreement with TEM observations could be caused by the grinding used to prepare a dispersion for TEM examination, which destroys the continuous anatase since carbon is mechanically stronger than anatase. The strong interaction of TiO_2 nanoparticles and polymer nanoparticles via hydrophilic groups, contributes to the small sizes of anatase (8–9 nm) and carbon nanoparticles and inhibits the growth of TiO_2 nanoparticles.

N_2 adsorption–desorption isotherms at −196°C are shown in Fig. 3a and the pore size distributions obtained using a DFT model are shown in Fig. 3b. The pore parameters are listed in Table 1. N_2 adsorption isotherms of the samples belong to Type II with reference to the IUPAC classification[41], which is typical of macroporous solids. These isotherms show a steep uptake at high relative pressures with no sign of levelling off due to capillary condensation mainly in the macropores. There is also a small steep uptake of N_2 at low relative pressures in the initial part of these isotherms, which can be attributed to micropore filling of N_2. The hysteresis loop of these samples is so small that it is hard to make an assignment, but it is approximately close to Type H3 according to the IUPAC[41] classification. Fig. 3b shows that there is small amount of mesopores. The volume of mesopores larger than 30 nm first increases then levels off with increasing $TiCl_4/(R + F)$ ratio. The volume of mesopores between 10 and 30 nm is the largest for TiO_2-C-3 and the volume of mesopores between 2 and 10 nm is the largest for TiO_2-C-1. There is no regular trend found for micropore sizes. The micropore volume of the hybrid aerogels exhibits a maximum of 0.043 cm^3/g at 0.720 with the $TiCl_4/(R + F)$ ratio as shown in Table 1. As macropore size is out of the detection range for nitrogen adsorption, we carried out mercury porosimetry to determine the macroporosity. The hybrid aerogels are not elastic, but stiff materials. There are no apparent compression stages in the uptake curves except for TiO_2-C-5 that has a small compression as shown in Fig. 3c. The mercury uptake abruptly increases at intrusion pressures from 50 to 400 psi with increasing $TiCl_4/(R + F)$ ratio. Therefore, the Washburn equation can be used to extract pore size distributions that are displayed in Fig. 3d. It can be seen that the pore sizes of the hybrid aerogels decrease from 966 to 167 nm with increasing $TiCl_4/(R + F)$ ratio from 0.629 to 1.261, which is in accordance with the trend from SEM

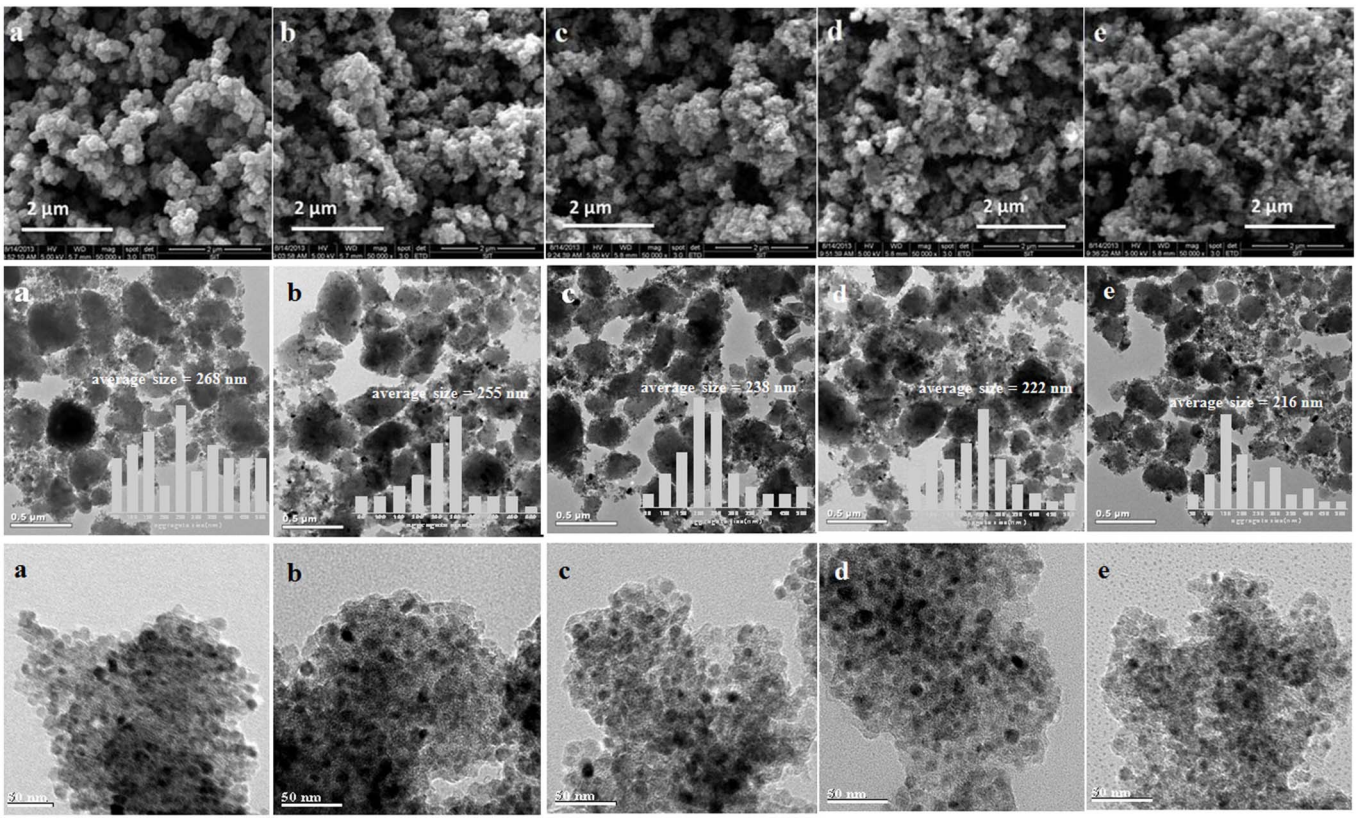

Figure 2 | SEM (top), TEM (middle) and HRTEM (bottom) images of the samples: a) TiO_2-C-1, b) TiO_2-C-2, c) TiO_2-C-3, d) TiO_2-C-4 and e) TiO_2-C-5.

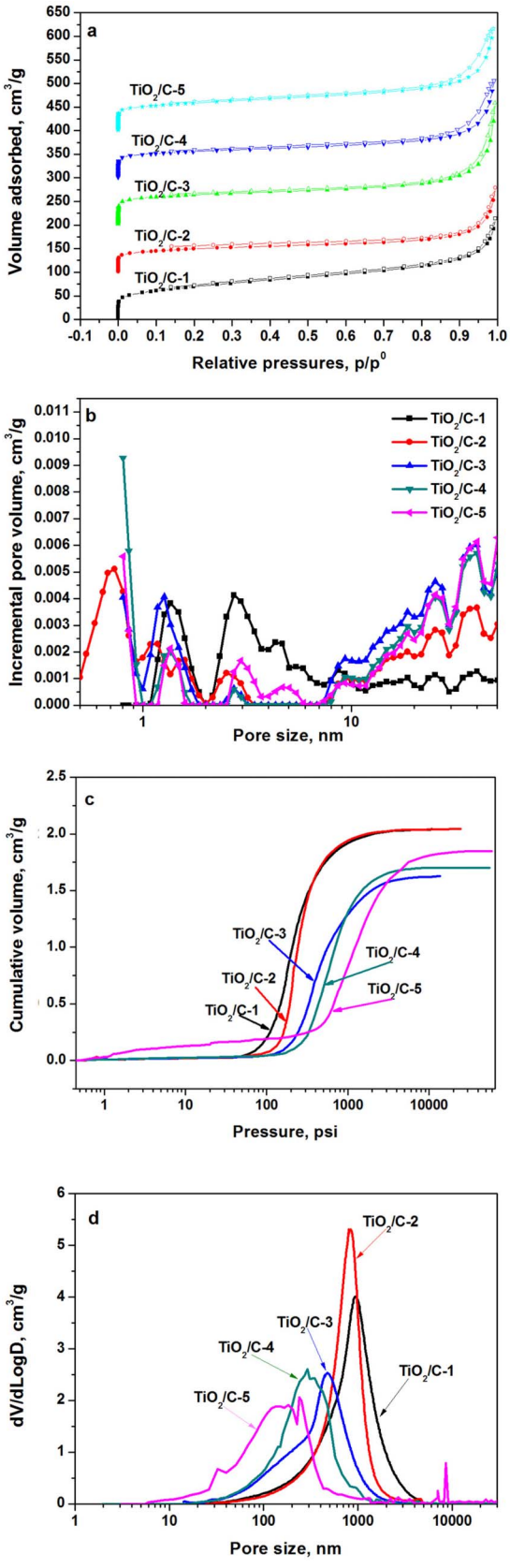

Figure 3 | Porous properties of the TiO_2-C hybrid aerogels. a) Nitrogen adsorption/desorption isotherms (the volume adsorbed is up-shifted 100, 200, 300 and 400 cm^3/g for samples TiO_2-C-2, TiO_2-C-3, TiO_2-C-4 and TiO_2-C5, respectively), b) Micro and mesopore size distributions from nitrogen adsorption using DFT model, c) Cumulative mercury intrusion and d) macropore size distributions from mercury porosimetry.

observations. From Table 1, we have found that the pore (>3.7 nm) volumes of the hybrid aerogels from mercury porosimetry exhibit a minimum of 1.62 cm^3/g at 0.902 (i. e. sample TiO_2-C-3) with increasing the $TiCl_4/(R + F)$ ratio. The macropore volumes are dominantly larger than the micropore or mesopore volumes, which agree well with the non-level off uptake of nitrogen in the adsorption isotherms (Fig. 3a). Therefore, the hybrid aerogels have dominant macropores with small amounts of micro and mesopores.

Photocatalytic activity. Photocatalytic degradation of MB in an aqueous suspension of the TiO_2-C hybrid aerogels was performed to evaluate their photocatalytic activity. Adsorption in the dark was also carried out in order to investigate the effect of adsorption on their photocatalytic activity. For comparison, adsorption and photodegradation of MB by P25 were also investigated under the same conditions. Fig. 4 shows the adsorption percentage for MB versus time in the dark and photocatalytic degradation percentage of MB versus time under UV light for the TiO_2-C hybrid aerogels and P25. Table 4 lists the kinetic parameters for MB adsorption and photocatalytic degradation. The MB adsorption follows a pseudo-second-order kinetics model for the first 180 min. The MB degradation-time curves can be well fitted by a first order kinetics model for 60 min. Above 60 min, a significant deviation from first order kinetics is observed. The adsorption of MB is the quickest and the equilibrium adsorption capacity is the smallest for P25. The adsorption capacity increases with increasing micropore volume except for TiO_2-C-1 because the dimensional size of the MB molecule (1.43 × 0.61 × 0.4 nm) is smaller than micropore size and the micropore has a relatively high adsorption potential. The exceptional high MB adsorption capacity of the TiO_2-C-1 can be attributed to its high volume of small mesopores (2–5 nm) as revealed by mesopore size distributions in Fig. 3b since the smaller mesopores (2–5 nm) contribute more surface area than the larger mesopores. Therefore, MB tends to be adsorbed preferentially in the micropores and small mesopores. The pseudo-second-order rate constants (k_2) are similar among the hybrid aerogels within experimental error. However the k_2 for P25 is four times higher than those of the hybrid aerogels, which can be ascribed to the short diffusion path for P25 (around 27 nm) while the particle size of the hybrid aerogels is of submicrometer scale.

The photocatalytic activities of the hybrid aerogels can be quantitatively evaluated by comparing the first order reaction rate constants (k_1). Direct comparison of the rate constants between the hybrid aerogels shows that they are markedly improved and vary widely compared with that of P25. This is due to the small particle size of anatase, a high loading level, reduced recombination of electron-hole pairs[11], and band gap narrowing[13]. The increasing order of the rate constants based on the weight of TiO_2 in the samples is TiO_2-C-4 < TiO_2-C-5 < TiO_2-C-2 < TiO_2-C-1 < TiO_2-C-3. The rate constant exhibit a maximum of 0.060 min^{-1} at 0.902 (TiO_2-C-3) with increasing $TiCl_4/(R + F)$ ratio, a value that is 4.23 times higher than that of P25 under the same conditions. The maximum rate ratio of TiO_2-C-3 to P25 is also much larger than that of TiO_2-GR5% and TiO_2-CNT5% to P25, which are 2.32 and 2.00 respectively as extracted from the curves in reference[13].

Optical properties. Fig. 4c shows the UV-vis diffuse reflectance spectra of the TiO_2-C hybrid aerogels. The presence of carbon induces increased light absorption in the visible region. A red shift to higher wavelengths in the absorption edge of the hybrid aerogels has also been observed, therefore indicating a narrowing of the band gap of TiO_2. It is difficult to determine the value of the red shifts because the background absorption ranging from 400 to 800 nm is very high. However, this red shift of our samples is higher than that of graphene-p25 nanocomposites by comparing the wavelengths at which curving of the lines by the superposition of TiO_2 and carbon absorption occurs (around 425 nm for our samples and 405 nm for

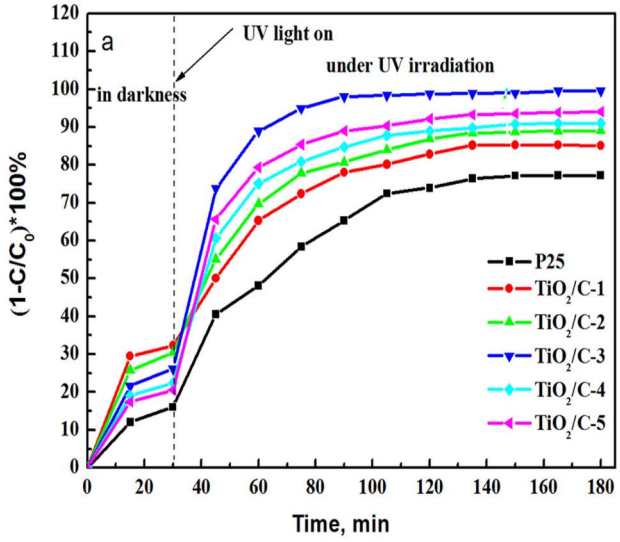

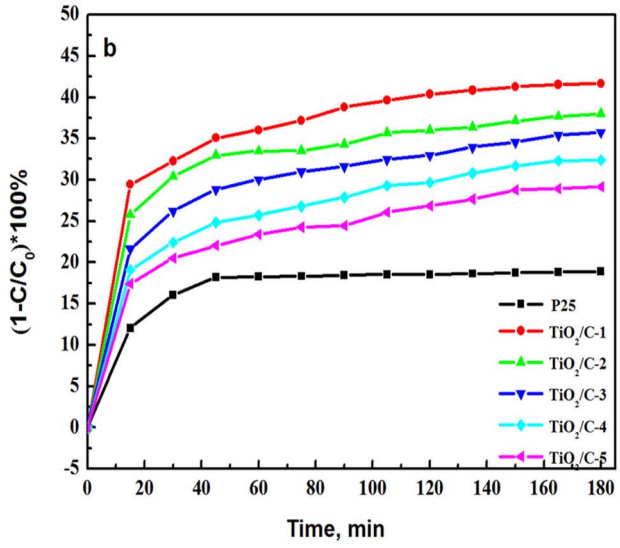

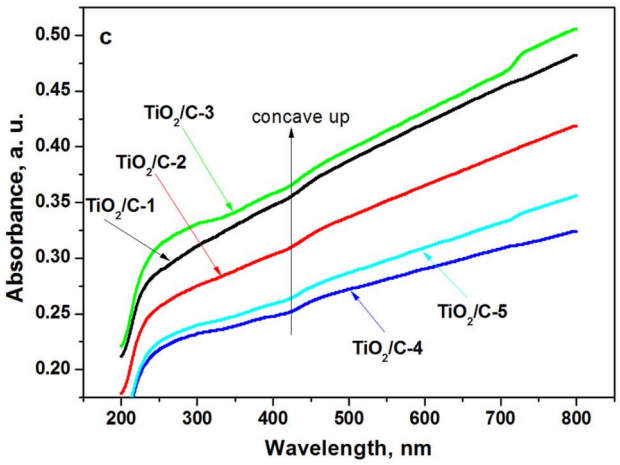

Figure 4 | a) Photocatalytic degradation of MB under the UV irradiation, b) Adsorption of MB in dark and c) UV-vis diffuse reflectance spectra of the TiO_2-C hybrid aerogels.

graphene-p25)[13]. In addition, the UV-vis diffuse reflectance increases in the following order: TiO_2-C-4 < TiO_2-C-5 < TiO_2-C-2 < TiO_2-C-1 < TiO_2-C-3. This is exactly that of the increasing order of the photocatalytic reaction rate constants normalized to the weights of TiO_2 in the samples. Therefore, light absorption by scattering is an important factor that determines the photocatalytic activity of the TiO_2-C hybrid aerogels.

Discussion

The structural formation mechanism of the hybrid aerogels can be understood as follows. The alcoholysis of $TiCl_4$ in the presence of the bidentate ligand, ethyl acetoacetate (EA), leads to the formation of $Ti(OEt)_3EA$. The condensed $Ti(OEt)_3EA$ forms inorganic colloid particles, growth of which is greatly inhibited compared with $Ti(OEt)_4$[42]. At the same time, the addition and condensation of resorcinol with furfural gives rise to organic nanoparticles under catalysis of in-situ formed HCl. Aggregation of inorganic and organic particles forms large submicrometer particles. Interaction among the submicrometer particles leads to a gelation of the solution and the formation of a macroporous gel. These pore structures are mostly retained after carbonization at 800°C since the polymers generated by the condensation of resorcinol with furfural are thermosetting. The interwoven structure of carbon and TiO_2 nanoparticles in the aggregates is caused by the strong hydrophilic interaction between TiO_2 colloidal particles and organic nanoparticles. The micropores are formed mainly in carbon nanoparticles during carbonization of the polymers by gas evolution. The mesopores are due to inter-nanoparticle voids and interstices between the contacting submicrometer particles. The macropores are formed by the inter-submicrometer particle voids.

The changing macropore size and volume with $TiCl_4/(R + F)$ ratio can be accounted for by this mechanism. As the RF concentration is fixed at a constant value for all the samples, increasing the $TiCl_4/(R + F)$ ratio leads to an increase of the total amount of TiO_2 and polymer nanoparticles, which favors a more robust gels formed at a higher $TiCl_4/(R + F)$ ratio. Therefore, the gels formed at a higher $TiCl_4/(R + F)$ ratio is more difficult to shrink during supercritical dying and carbonization than that at a lower $TiCl_4/(R + F)$ ratio. This factor leads to an increase of pore volume with $TiCl_4/(R + F)$ ratio. On the other hand, an increase of $TiCl_4/(R + F)$ ratio could cause a decrease in the total pore volume if judged merely by the volume filling effect of the submicrometer particles. Also, the smaller the submicrometer particle, the higher the driving forces for coarsening after gelation and sintering during carbonization and these decrease the pore volume with increasing $TiCl_4/(R + F)$ ratio. Therefore, theses opposing actions cause a minimum of total pore volumes with increasing $TiCl_4/(R + F)$ ratio.

Adsorption kinetics is not the main factor that contributes to the difference of the photocatalytic activities as it suggests a similar rate constant, which is ascribed to a the hierarchical macro, meso and micropores. Adsorption of MB can decrease the diffusion path of MB to TiO_2 nanoparticles by surface diffusion and increase photocatalytic activities for all samples. As the carbon and TiO_2 nanoparticles are evenly distributed and interwoven with each other at the nanometer scale, the interfacial diffusion rate of MB from carbon pore walls to the hydrophilic external surface of TiO_2 active centers should be high. The macropore sizes and volumes also cannot explain the quite different apparent reaction rate constants. The TiO_2-C-3 has a minimum total pore volume, which seems inconsistent with it having the maximum apparent reaction rate constant. The macropore size decreases with increasing $TiCl_4/(R + F)$ ratio, which should result in a decreased diffusion rate with increasing the $TiCl_4/(R + F)$ ratio and therefore a decreased reaction rate constant. This is apparently not what happens. Neither can mesopore volume rationalize the maximum reaction rate constant because TiO_2-C-5 has a comparable mesopore volume to TiO_2-C-3, but the rate constant of the former is significantly lower than that of the latter.

The crystallinity and crystallite size of the TiO_2 nanoparticles are all similar within experimental error for the hybrid aerogels, and therefore do not account for the different photocatalytic activities. The smaller the submicrometer particle, the higher is percentage of

Table 4 | Adsorption kinetics and photocatalytic activities of the TiO_2-C hybrid aerogels

	P25	TiO_2-C-1	TiO_2-C-2	TiO_2-C-3	TiO_2-C-4	TiO_2-C-5
q_2, mg/g	3.91 ± 0.03	8.83 ± 0.08	7.93 ± 0.10	7.61 ± 0.11	7.08 ± 0.15	6.36 ± 0.15
$k_2 \times 10^{-2}$, min·g/mg	4.4 ± 0.8	1.0 ± 0.1	1.2 ± 0.2	0.9 ± 0.1	0.7 ± 0.1	0.8 ± 0.2
r_{22}	0.99	0.99	0.99	0.99	0.99	0.99
$k_1 \times 10^{-2}$, min^{-1}	1.4 ± 0.1	1.9 ± 0.1	2.2 ± 0.2	6.0 ± 0.2	2.6 ± 0.4	3.2 ± 0.4
r_{12}	0.97	0.98	0.96	0.99	0.94	0.94
Rate ratio to P25	1.00 ± 0.00	1.34 ± 0.04	1.54 ± 0.03	4.23 ± 0.22	1.87 ± 0.03	2.26 ± 0.10

TiO_2 exposed to UV light. As the sizes of submicrometer particles decrease and weight percentages of TiO_2 increase with increasing $TiCl_4$/(R + F) ratio, the amount of the exposed TiO_2 nanoparticles and photodegradation activity should increase accordingly. This can explain the increasing rate constant with increasing $TiCl_4$/(R + F) ratio except for sample TiO_2-C-3 with the experimentally-observed maximum.

Since oxygen vacancies in anatase are preferably located at the subsurface[7], the high percentage of oxygen vacancies (7.2–18%) in our samples can be ascribed to the small size of the TiO_2 because a size decrease of TiO_2 nanoparticles favors an increase in subsurface area. Carbon thermal reduction is another factor that our samples have high oxygen vacancies in TiO_2. The minimum oxygen vacancy for TiO_2-C-3 could be caused by coarsening and sintering that increases surface contact between anatase nanoparticles, which decreases subsurface area. This is could be accounted for by the following two opposing factors. On the one hand, the interaction between polymer nanoparticles, (precursors of the carbon nanostructure) and the TiO_2 nanoparticles decreases with increasing $TiCl_4$/(R + F) ratio, therefore, the interaction between TiO_2 nanoparticles increases, leading to an increase of coarsening and sintering during aging and carbonization. One the other hand, with increasing $TiCl_4$/(R + F) ratio, the amount of catalytic HCl generated increases, the addition and polymerization rate of resorcinol with furfural increases, the cross-linking density of the polymer increases, the size of the polymer nanoparticles decreases and the interaction of polymer nanoparticles with TiO_2 nanoparticles increases, leading to a decrease of coarsening and sintering during aging and carbonization. As a compromise result, the coarsening and sintering during the aging and carbonization of TiO_2 nanoparticles reach a maximum with $TiCl_4$/(R + F) ratio, and oxygen vacancy concentration exhibits a minimum because coarsening and sintering of TiO_2 nanoparticles decrease the anatase subsurface area. The minimum O/C ratio in carbon is another indication that interaction between carbon and TiO_2 nanoparticles reaches a minimum at 0.902 (i. e. sample TiO_2-C-3) with $TiCl_4$/(R + F) ratio as carbon nanoparticles can reduce TiO_2 particles and increase oxygen vacancy in TiO_2.

It has long been established that TiO_2 surfaces containing O vacancies exhibit a higher catalytic activity than defect-free surfaces to reactions such as the dissociation of water[43]. However, it is argued[44] that photocatalytic activity is enhanced by a good mixing between Ti and O states around the Fermi energy. These effects act in opposition, in turn suggesting that there is an optimum defect concentration for activity in photocatalysis, above and below which activity should decrease. As our samples have high oxygen vacancy concentrations, it might be possible that these defect concentrations are all above the optimum value and therefore TiO_2-C-3 with the lowest oxygen vacancy concentration has the highest photocatalytic activity among our samples.

The maximum reaction rate can be ascribed to the maximum absorption of UV light due to the pore scattering as explained below. According to the Beer-Lambert law, the light intensity percentage passing through a sample can be calculated by equation (1).

$$\frac{I}{I_0} \times 100\% = (1-R)^2/\exp[(\beta+S)x] \quad (1)$$

Where $\frac{I}{I_0} \times 100\%$ is the light intensity percentage passing through the sample, R the reflectance, β the absorption coefficient caused by the electron excitement, x the light transmission length and S the scattering coefficient. The greater the light intensity passing through the sample, the lower the light absorption in the sample. The absorption coefficient is independent of the pore structure of the hybrid aerogels while the scattering coefficient depends on the pore size and size distribution. Since the wavelength (λ = 365 nm) of UV light is comparable to the macropore sizes, the samples show different scattering properties. When the pore size increases and is close to the wavelength of UV light, the scattering changes from forward scattering to large angle scattering. On the other hand, large size pores mainly contribute backward scattering. The large angle scattering will enhance the absorption since more light propagates inside the sample. There is an optimum pore size (d_{max}) described by the equation (2), at which light scattering and absorption reach a maximum.

$$d_{\max} = \frac{4.1\lambda}{2\pi(n-1)} \quad (2)$$

Where λ is the UV wavelength and n the relative index of refraction. Therefore, the maximum rate constant may be ascribed to a maximum light absorption from macropore scattering since the macropore size of the TiO_2-C-3 is close to the optimum pore size. The difference in the UV-vis diffuse reflectance of TiO_2-C-3 compared to the other samples is not as large as the difference in their reaction rate constants. This might be caused by light absorption by the sample.

The percentage of TiO_2 nanoparticles exposed to UV light in the submicrometer particles can be estimated by their sizes and light penetrating depth. The absorption of light incident on 8–9 nm carbon nanoparticles is estimated to be around 54–61% since single layer graphene has a light absorption of 2.3%[45]. Therefore, the light penetrating depth of UV light in submicrometer particles is around 15 nm, which means that if 100% of the TiO_2 particles were reached by the UV light, the sizes of the secondary aggregates would have to be less than 30 nm. In light of the fact that the hybrid TiO_2-C aerogels have secondary aggregated particles from 216 to 268 nm, the utilization ratio of TiO_2 particles in terms of light penetrability is rather low, and photocatalytic activity of the TiO_2 nanoparticles is extremely high. This indicates that a further significant increase of photocatalytic activity is possible by decreasing the aggregate size.

In summary, we have synthesized novel TiO_2-C hybrid aerogels, in which anatase TiO_2 and carbon nanoparticles are interwoven to form submicrometer aggregates that form macroporous pores with sizes tunable from 966 to 166 nm. The oxygen vacancy concentration in the anatase TiO_2 nanoparticles is between 7.2 to 18.0% and the size of the TiO_2 nanoparticles is around 8–9 nm. Reduced electron-hole recombination, small particle size, high oxygen vacancy concentration, reduced band gap, a short diffusion path for the reactant and pore scattering are responsible for the high photocatalytic activity of the hybrid aerogels. The highest photocatalytic activity of TiO_2-C-3 is due to an optimum macropore size that can increase light utilization by pore scattering and possibly an appropriate oxygen vacancy concentration.

Methods

Preparation. All the reagents were analytical grade and used as received. 10 g of resorcinol (R) and furfural (F) with a molar ratio of 1 : 2 was mixed under stirring to form a clear solution A. Anhydrous ethanol and ethyl acetoacetate (EA) was mixed in an ice bath to form a solution, to which $TiCl_4$ was first dropped slowly under rigorous agitation and thereafter propylene oxide (PO) was added drop-wise to form a solution B. Finally, solution A was added drop-wise to solution B with rigorous stirring at room temperature. The formulations of the samples were determined as following. The amounts of resorcinol and furfural were kept the same as above. The mass ratios of $TiCl_4$/(R + F) were 0.629, 0.720, 0.902, 1.171 and 1.261 for the five samples. The amount of EA and PO was calculated by keeping the same molar ratios of PO/Ti and EA/Ti at 6 and 0.6, respectively. The total mass of resorcinol, furfural, anhydrous ethanol, EA and PO was 100 g and the amount of anhydrous ethanol was calculated from the mass balance. The five samples were named TiO_2-C-1, TiO_2-C-2, TiO_2-C-3, TiO_2-C-4 and TiO_2-C-5 with increasing mass ratio of $TiCl_4$/(R + F). After completing the above process, the final solution was agitated for 10 min, transferred to ampoules (30 ml each) and sealed by a gas torch. The sealed ampoules were placed in a water bath at 70°C for 5 days to form the TiO_2-RF wet gels, and were then broken and put into in a n-hexane-filled autoclave to carry out supercritical drying at 240°C and 6 MPa for 1 hour, afterwards the autoclave was depressurized at a rate of 0.1 MPa/min to atmosphere pressure and cooled to room temperature naturally. The dried TiO_2-RF hybrid aerogels were carbonized in a vertical tube furnace at 800°C for 3 hours to obtain the hybrid TiO_2-C aerogels using a heating rate of 2°C/min under a nitrogen flow.

Microstructure characterization. TiO_2 content was calculated based on weight loss determined by burning the TiO_2-C hybrid aerogels at 800°C in air for 3 h. The X-ray diffraction (XRD) patterns of the samples were collected on a D/MAX 2000/PC diffractometer (Rigaku, Japan) with Cu Kα radiation. The accelerating voltage and the applied current were 40 kV and 40 mA, respectively. The crystallite size of TiO_2 was calculated using the Scherrer equation based on the (101) diffraction peak of anatase. Transmission electron microscope (TEM) and scanning electron microscope (SEM) images were collected by using a JEM 2010 EX microscope (JEOL, Japan) and a Scanning Electron Microscope Quanta 200 FEG (FEI Co., USA) with accelerating voltages of 30 and 200 KeV, respectively. The histograms of aggregate sizes were obtained by measuring the sizes and counting the numbers of the aggregated particles. Nitrogen adsorption and desorption isotherms of samples were obtained on a Tristar physical adsorption apparatus (Micromeritics Corp., USA) at 77 K. Surface areas of samples were determined by applying adsorption data of p/p° between 0.01 and 0.26 to the Brunauer Emmett Teller (BET) equation. Pore size distributions were obtained by a non-local density functional theory (DFT) model, assuming a slit pore geometry. Micropore and mesopore volumes were estimated by the DFT method for pores with volumes less than 2 nm and between 2 and 50 nm. The external surface areas were obtained by the t-plot method. Mercury intrusion porosimetry of monolithic TiO_2-C hybrid aerogels was carried out in the chamber of an AutoPore IV 9500 porosimeter (Micromeritics Corp., USA). After the chamber was evacuated to 20 Pa, mercury was introduced to the chamber, the hydrostatic head of which yielded an initial low pressure of 3 kPa. Pressure was subsequently increased to a maximum pressure of approximately 400 MPa. The pressure increments were chosen to correspond to even intervals on a logarithmic scale. After each pressure increment, the machine was set to "pause" to allow the pressure and volume readings to stabilize before recording a pressure/volume data pair. The Washburn equation ($r = -2\gamma cos\theta/P$) was used to extract pore size distributions by assuming a Hg surface tension (γ) of 480 mN/m and a contact angle (θ) of Hg with the samples of 140°. The total pore volume from mercury porosimetry measurements was read from the curve of cumulative pore volume versus intrusion pressure. XPS spectra were recorded on a ESCALAB250Xi X-ray photoelectron spectrometer (Thermo Fisher Scientific, USA) using AlKa radiation (1486.6 eV) and operating at 150 W. All binding energies were calibrated based on the C 1s line (284.6 eV) of adventitious carbon. The XPS analysis was done at ambient temperature and the base pressure in the measurement chamber was on the order of less than 10^{-8} Pa. Prior to analysis, the samples were outgassed in a vacuum oven overnight. The CASA XPS program with a Gaussian-Lorentzian mix function and Shirley background subtraction was used to deconvolute the XPS spectra. Raman spectra were obtained on a DXR Raman spectrometer (Thermo Fisher Scientific, USA) equipped with a charge-coupled device detector. The excitation source used was an Ar ion laser (λ = 514.5 nm) with a spot size of approximately 1 mm. The power of the incident beam on the sample was 3 mW. The time of acquisition was adjusted according to the intensity of the Raman scattering. The wavenumber values reported from the spectra are accurate within 2 cm^{-1}. The optical properties of the samples were analyzed by UV-vis diffuse reflectance spectroscopy (UV-vis DRS) using a Cary-100 UV-vis spectrophotometer (Varian Co., USA), in which $BaSO_4$ was used as the background.

Adsorption and photocatalytic activity. The photocatalytic degradation of MB was performed in a stirred quartz reactor filled with 50 ml MB aqueous solution (20 ppm). The catalyst (50 mg, 80–100 mesh) was loaded in the reactor equipped with 500 W UV lamps with a wavelength centered at 365 nm as the light source. All of the photocatalytic experiments were carried out after the adsorption of MB in the dark for 30 min under stirring. Under ambient conditions and rigorous stirring, the reactor was exposed to the UV irradiation. A 3 mL sample solution was taken at certain time intervals during the experiment and centrifuged to remove the catalyst completely. The solution was analyzed on a Cary-100 UV-vis spectrophotometer (Varian Co., USA). The MB degradation percentages, (1-C/C_0)*100% are plotted with time. Here, C is the concentration of MB in solution at each irradiation time interval, while C_0 is the initial concentration. For a comparison of adsorption with photo degradation, MB adsorption in the dark was carried out with the same procedure as the photocatalytic experiments described above, but with no UV lamps turned on. The percentage removal by adsorption is reported as (1-C/C_0)*100% with time. For a comparison of our samples with commercial sample, P25, a commercial TiO_2 photocatalyst supplied by Degussa GmbH, Germany, was tested for its adsorptivity and photocatalytic degradation of MB using the same procedure and conditions given above. The MB adsorption kinetics data and the MB degradation kinetics data were fitted by a pseudo-second-order model and the Lagergren pseudo first-order model respectively[46]. The Lagergren pseudo first-order model and the pseudo-second-order model can be described by the equations (3) and (4) respectively.

$$\log(q_t - q_e) = \log q_e - \frac{k_1}{2.303} t \tag{3}$$

Where t is time in min, q_t the amount of MB degraded at t in mg/g, qe the amount of MB degraded at equilibrium in mg/g, and k_1 the first-order rate constant in min^{-1}. We can obtain k_1 by applying MB photodegradation kinetics data to equation (3). The correlation coefficients r_{12}, values and standard errors (SE) of the fit were extracted.

$$\frac{t}{q_t} = \frac{1}{k_2 q_2^2} + \frac{1}{q_2} t \tag{4}$$

Where t is time in min, q_t the amount of MB adsorbed at t in mg/g, q_2 the amount of MB adsorbed at equilibrium in mg/g, and k_2 the pseudo-second-order rate constant in min·g/mg. We can obtain k_2 and q_2 by applying MB adsorption kinetics data in the dark to equation (4). The correlation coefficients r_{22}, values and standard errors (SE) of the fit were also extracted.

1. Inagaki, M., Nonaka, R., Tryba, B. & Morawski, A. W. Dependence of photocatalytic activity of anatase powders on their crystallinity. *Chemosphere.* **64**, 437–445 (2006).
2. Xu, N., Shi, Z., Fan, Y., Dong, J. & Shi, J. Effects of particle size of TiO_2 on photocatalytic degradation of MB in aqueous suspensions. *Ind. Eng. Chem. Res.* **38**, 373–379 (1999).
3. Sakai, N., Wang, R., Fujishima, A. & Watanabe, T. Effect of ultrasonic treatment on highly hydrophilic TiO_2 surfaces. *Langmuir.* **14**, 5918–5920 (1998).
4. Tryba, B. *et al.* Photocatalytic activity and OH radical formation on TiO_2 in the relation to crystallinity. *Appl. Catal. B-Environ.* **71**, 163–168 (2007).
5. Mao, Y. B. & Wong, S. S. Size and shape-dependent transformation of nanosizedtitanate into analogous anatasetitania nanostructures. *J. Am. Chem. Soc.* **128**, 8217–8226 (2006).
6. Lin, Z., Orlov, A., Lambert, R. M. & Payne, M. C. New insights into the origin of visible light photocatalytic activity of nitrogen-doped and oxygen-deficient anatase TiO_2. *J. Phys. Chem. B.* **109**, 20948–20952 (2005).
7. Cheng, H. Z. & Selloni, A. Surface and subsurface oxygen vacancies in anatase TiO_2 and differences with rutile. *Phys. Rev. B* **79**, 092101 (2009).
8. Minero, C., Catozzo, F. & Pelizzetti, E. Role of adsorption in photocatalyzed reactions of organic molecules in aqueous titania suspensions. *Langmuir.* **8**, 481–486 (1992).
9. Torimoto, T., Ito, S. & Kuwabata, S. Effects of adsorbents used as supports for titanium dioxide loading on photocatalytic degradation of propyzamide. *Envrion. Sci. Technol.* **30**, 1275–1281 (1996).
10. Tsumura, T., Kojitani, N., Izumi, I. & Iwashita, N. Carbon coating of anatase-type TiO_2 and photoactivity. *J. Mater. Chem.* **12**, 1391–1396 (2002).
11. Zhou, K. F., Zhu, Y. H., Yang, X. L., Jiang, X. & Li, C. Z. Preparation of graphene–TiO_2 composites with enhanced photocatalytic activity. *New J. Chem.* **35**, 353–359 (2011).
12. Zang, L. *et al.* Visible-light detoxification and charge generation by transition metal chloride modified titania. *Chem. Euro. J.* **6**, 379–384 (2000).
13. Zhang, Y. H., Tang, Z. R., Fu, X. Z. & Xu, Y. J. TiO_2-graphene nanocomposites for gas-phase photocatalytic degradation of volatile aromatic pollutant: Is TiO_2-graphene truly different from other TiO_2-carbon composite materials? *ACS nano.* **4**, 7303–7314 (2010).
14. Irie, H., Watanabe, Y. & Hashimoto, K. Carbon-doped anatase TiO_2 powders as a visible-light sensitive photocatalyst. *Chem. Lett.* **32**, 772–773 (2003).
15. Nakamura, R., Tanaka,T. & Nakato, Y. Mechanism for visible light responses in anodic photocurrents at N-doped TiO_2 film electrodes. *J. Phys. Chem. B.* **108**, 10617–10620 (2004).
16. Sakthivel, S. & Kisch, H. Daylight photocatalysis by carbon-modified titanium dioxide. *Angew. Chem. Int. Ed.* **42**, 4908–4911 (2003).
17. Toyoda, M. *et al. Carbon materials in photocatalysis.* Chapter in "**Chemistry and physics of carbon**" (edited by Radovic, L.), Taylor & Francis Group, CRC Press Boca Rato, Floride, USA,Vol. **31**, p171–249 (2013).
18. Carp, O., Huisman, C. L. & Reller, A. Photoinduced reactivity of titanium dioxide. *Prog. Solid State Chem.* **32**, 33–177 (2004).
19. Chen, M. L., Lim, C. S. & Oh, W. C. Preparation with different mixing ratios of anatase to activated carbon and their photocatalytic performance. *J. Ceram. Process. Res.* **8**, 119–124 (2007).

20. Matos, J., Laine, J. & Herrmann, J. M. Synergy effect in the photocatalytic degradation of phenol on a suspended mixture of titania and activated carbon. *Appl. Catal. B-Environ.* **18**, 281–291 (1998).
21. Yuan, R. S., Guan, R. B., Shen, W. Z. & Zheng, J. T. Photocatalytic degradation of MB by a combination of TiO_2 and activated carbon fibers. *J. Colloid Interf. Sci.* **282**, 87–91 (2005).
22. Inagaki, M., Kojin, F., Tryba, B. & Toyoda, M. Carbon-coated anatase: the role of the carbon layer for photocatalytic performance. *Carbon.* **43**, 1652–1659 (2005).
23. Ohno, T., Tsubota, T., Nishijima, K. & Miyamato, Z. Degradation of MB on carbonate species-doped TiO_2 photocatalysts under visible light. *Chem.lett.* **33**, 750–751 (2004).
24. Toyoda, M., Yano, T., Tomoki, T., Amao, Y. & Inagaki, M. Effects of carbon coating on Ti_nO_{2n-1} for decomposition of iminoactadine triacetate in aqueous solution under visible light. *J. Adv. Oxid. Technol.* **9**, 49–52 (2006).
25. Toyoda, M. *et al.* Preparation of carbon-coated Magneli phases Ti_nO_{2n-1} and their photocatalytic activity under visible light. *Appl. Catal. B-Environ.* **88**, 160–164 (2009).
26. Woan, K., Pyrgiotakis, G. & Sigmund, W. Photocatalytic carbon canotube-TiO_2 composites. *Adv. Mater.* **21**, 2233–2239 (2009).
27. Tryba, B., Morawski, A. W., Tsumura, T., Toyoda, M. & Inagaki, M. Hybridization of adsorptivity with photocatalytic activity–carbon-coated anatase. *J. Photoch. Photobio. A.* **167**, 127–135 (2004).
28. Puma, G. L., Bono, A., Krishnaiah, D. & Collin, J. G. Preparation of titanium dioxide photocatalyst loaded onto activated carbon support using chemical vapor deposition: A review paper. *J. Hazard.Mater.* **157**, 209–219 (2008).
29. Uchida, H., Itoh, S. & Yoneyama, H. Photocatalytic decomposition of propyzamide using TiO_2 supported on activated carbon. *Chem. Lett.* **22**, 1995–1998 (1993).
30. El-Sheikh, A. H. *et al.* Deposition of anatase on the surface of activated carbon. *Surf. Coat. Technol.* **187**, 284–292 (2004).
31. Arana, J. *et al.* TiO_2 activation by using activated carbon as a support. I. Surface characterization and decantability study. *Appl. Catal. B-Environ.* **44**, 161–172 (2003).
32. Tryba, B., Tsumura, T., Janus, M., Morawski, A. W. & Inagaki, M. Carbon-coated anatase: adsorption and decomposition of phenol in water. *Appl. Catal. B-Environ.* **50**, 177–183 (2004).
33. Akpan, U. G. & Hameed, B. H. Parameters affecting the photocatalytic degradation of dyes using TiO_2-based photocatalysts: A review. *J. Hazard. Mater.* **170**, 520–529 (2009).
34. Gao, B., Chen, G. Z. & Puma, G. L. Carbon nanotubes/titanium dioxide (CNTs/TiO_2) nanocomposites prepared by conventional and novel surfactant wrapping sol–gel methods exhibiting enhanced photocatalytic activity. *Appl. Catal. B-Environ.* **89**, 503–509 (2009).
35. Zhang, W. F., He, Y. L., Zhang, M. S., Yin, Z. & Chen, Q. Raman scattering study on anatase TiO_2 nanocrystals. *J. Phys. D: Appl. Phys.* **33**, 912–916 (2000).
36. Parker, J. C. & Siegel, R. W. Calibration of the Raman spectrum to the oxygen stoichiometry of nanoparticle TiO_2. *Appl. Phys. Lett.* **57**, 943–945 (1990).
37. Ohsaka, T., Yamaoka, S. & Shimomura, O. Effect of hydrostatic pressure on the Raman spectrum of anatase (TiO_2). *Solid State Commun.* **30**, 345–347 (1979).
38. Södergren, S. *et al.* Lithium intercalation in nanoporous anatase TiO_2 studied with XPS. *J. Phys. Chem. B.* **101**, 3087–3090 (1997).
39. Milošv, I., Strehblow, H. H., Navinšek, B. & Metikoš-Huković, M. Electrochemical and thermal oxidation of TiN coating studied by XPS. *Surf. Interface Anal.* **23**, 529–539 (1995).
40. Han, P. X. *et al.* Graphene oxide nanosheets/multi-walled carbon nanotubes hybrid as an excellent electrocatalytic material towards VO^{2+}/VO_2^+ redox couples for vanadium redox flow batteries. *Energy Environ. Sci.* **4**, 4710–4717 (2011).
41. Singh, K. S. W. *et al.* Reporting physisorption data for gas/solid systems with special reference to the determination of surface area and porosity. *Pure Appl. Chem.* **57**, 603–619 (1985).
42. Leaustic, A., Babonneau, F. & Livage, J. Structural investigation of the hydrolysis-condensation process of titanium alkoxides $Ti(OR)_4$ (OR = OPri, OEt) modified by acetylacetone. 2. from the modified precursor to the colloids. *Chem. Mat.* **1**, 248–252 (1989).
43. Henderson, M. A., Epling, W. S., Peden, C. H. F. & Perkin, C. L. Insights into photoexcited electron scavenging processes on TiO_2 obtained from studies of the reaction of O2 with OH groups adsorbed at electronic defects on TiO_2(110). *J. Phys. Chem. B.* **107**, 534–545 (2003).
44. Thomas, A. G. *et al.* Comparison of the electronic structure of anatase and rutile TiO_2 single-crystal surfaces using resonant photoemission and x-ray absorption spectroscopy. *Phys. Rev. B.* **75**, 035105 (2007).
45. Nair, R. R. *et al.* Fine structure constant defines visual transparency of graphene. *Science.* **320**, 1308 (2008).
46. Ho, Y. S. & McKay, G. Sorption of dye from aqueous solution by peat. *Chem. Eng. J.* **70**, 115–124 (1998).

Acknowledgments

This work was financially supported by the Capacity Building Program of Shanghai local universities (No. 12160503600), the first-class discipline construction fund of Shanghai municipal education commission (No.J201212), Nature Science Foundation of China (50872033, 11079041, U1332107) and the key subject of Materials processing projects (No. J51504). The authors thank Prof. Ping Yu at Physics & Astronomy Department, University of Missouri-Columbia for helpful and instructive discussion.

Author contributions

R.Z. and W.C.L. conceived and designed the experiments, R.Z. and X.S. co-wrote the paper, X.S. and F.P. conducted the material synthesis and accomplished the characterizations including XRD, XPS, Raman, SEM, TEM, nitrogen adsorption, mercury porosimetry and UV-vis diffuse reflectance experiments, R.Z. and X.S. carried out photocatalytic activity experiment. All authors discussed the results and commented on the manuscript.

Additional information

Supplementary information accompanies this paper at http://www.nature.com/scientificreports

Competing financial interests: The authors declare no competing financial interests.

How to cite this article: Shao, X., Lu, W.C., Zhang, R. & Pan, F. Enhanced photocatalytic activity of TiO_2-C hybrid aerogels for methylene blue degradation. *Sci. Rep.* **3**, 3018; DOI:10.1038/srep03018 (2013).